

1

<sup>2</sup>A SEARCH FOR LONG-LIVED, CHARGED, SUPERSYMMETRIC PARTICLES  
<sup>3</sup>USING IONIZATION WITH THE ATLAS DETECTOR

4

BRADLEY AXEN

5

September 2016 – Version 0.21

6



<sup>8</sup> Bradley Axen: *A Search for Long-Lived, Charged, Supersymmetric Particles using Ion-  
<sup>9</sup> ization with the ATLAS Detector*, Subtitle, © September 2016

<sup>10</sup>

Usually a quotation.

<sup>11</sup>

Dedicated to.



<sub>12</sub> ABSTRACT

---

<sub>13</sub> How to write a good abstract:

<sub>14</sub> <https://plg.uwaterloo.ca/~migod/research/beck00PSLA.html>



<sub>15</sub> PUBLICATIONS

---

<sub>16</sub> Some ideas and figures have appeared previously in the following publications:

<sub>17</sub>

<sub>18</sub> Put your publications from the thesis here. The packages `multibib` or `bibtopic`  
<sub>19</sub> etc. can be used to handle multiple different bibliographies in your document.



---

<sup>21</sup> ACKNOWLEDGEMENTS

<sup>22</sup> Put your acknowledgements here.

<sup>23</sup>

<sup>24</sup> And potentially a second round.

<sup>25</sup>



26 CONTENTS

---

27	I	INTRODUCTION	1
28	1	INTRODUCTION	3
29	II	THEORETICAL CONTEXT	5
30	2	STANDARD MODEL	7
31	2.1	Particles . . . . .	7
32	2.2	Interactions . . . . .	8
33	2.3	Limitations . . . . .	8
34	3	SUPERSYMMETRY	9
35	3.1	Motivation . . . . .	9
36	3.2	Structure . . . . .	9
37	3.3	Phenomenology . . . . .	9
38	4	LONG-LIVED PARTICLES	11
39	4.1	Mechanisms . . . . .	11
40	4.1.1	Examples in Supersymmetry . . . . .	11
41	4.2	Phenomenology . . . . .	11
42	4.2.1	Disimilarities to Prompt Decays . . . . .	11
43	4.2.2	Characteristic Signatures . . . . .	11
44	III	EXPERIMENTAL STRUCTURE AND RECONSTRUCTION	13
45	5	THE LARGE HADRON COLLIDER	15
46	5.1	Injection Chain . . . . .	15
47	5.2	Design and Parameters . . . . .	15
48	5.3	Luminosity . . . . .	15
49	6	THE ATLAS DETECTOR	17
50	6.1	Coordinate System . . . . .	17
51	6.2	Magnetic Field . . . . .	17
52	6.3	Inner Detector . . . . .	17
53	6.3.1	Pixel Detector . . . . .	17
54	6.3.2	Semiconductor Tracker . . . . .	17
55	6.3.3	Transition Radiation Tracker . . . . .	17
56	6.4	Calorimetry . . . . .	17
57	6.4.1	Electromagnetic Calorimeters . . . . .	17
58	6.4.2	Hadronic Calorimeters . . . . .	17
59	6.4.3	Forward Calorimeters . . . . .	17
60	6.5	Muon Spectrometer . . . . .	17
61	6.6	Trigger . . . . .	17
62	6.6.1	Trigger Scheme . . . . .	17
63	6.6.2	Missing Transverse Energy Triggers . . . . .	17
64	7	EVENT RECONSTRUCTION	19
65	7.1	Tracks and Vertices . . . . .	19

66	7.1.1	Track Reconstruction . . . . .	19
67	7.1.2	Vertex Reconstruction . . . . .	19
68	7.2	Jets . . . . .	19
69	7.2.1	Topological Clustering . . . . .	19
70	7.2.2	Jet Energy Scale . . . . .	19
71	7.2.3	Jet Energy Scale Uncertainties . . . . .	19
72	7.2.4	Jet Energy Resolution . . . . .	19
73	7.3	Electrons . . . . .	19
74	7.3.1	Electron Identification . . . . .	19
75	7.4	Muons . . . . .	19
76	7.4.1	Muon Identification . . . . .	19
77	7.5	Missing Transverse Energy . . . . .	19
78	IV	CALORIMETER RESPONSE	21
79	8	RESPONSE MEASUREMENT WITH SINGLE HADRONS	23
80	8.1	Dataset and Simulation . . . . .	24
81	8.1.1	Data Samples . . . . .	24
82	8.1.2	Simulated Samples . . . . .	24
83	8.1.3	Event Selection . . . . .	24
84	8.2	Inclusive Hadron Response . . . . .	25
85	8.2.1	E/p Distribution . . . . .	26
86	8.2.2	Zero Fraction . . . . .	26
87	8.2.3	Neutral Background Subtraction . . . . .	27
88	8.2.4	Corrected Response . . . . .	28
89	8.3	Identified Particle Response . . . . .	34
90	8.3.1	Decay Reconstruction . . . . .	34
91	8.3.2	Identified Response . . . . .	35
92	8.3.3	Additional Species in Simulation . . . . .	37
93	8.4	Summary . . . . .	38
94	9	JET ENERGY RESPONSE AND UNCERTAINTY	41
95	9.1	Motivation . . . . .	41
96	9.2	Uncertainty Estimate . . . . .	41
97	9.3	Summary . . . . .	43
98	V	SEARCH FOR LONG-LIVED PARTICLES	47
99	10	LONG-LIVED PARTICLES IN ATLAS	49
100	10.1	Overview and Characteristics . . . . .	49
101	10.2	Simulation . . . . .	49
102	11	EVENT SELECTION	51
103	11.1	Trigger . . . . .	51
104	11.2	Kinematics and Isolation . . . . .	51
105	11.3	Standard Model Rejection . . . . .	51
106	11.4	Ionization . . . . .	51
107	11.4.1	dE/dx Calibration . . . . .	51
108	11.4.2	Mass Estimation . . . . .	51
109	12	BACKGROUND ESTIMATION	53

110	12.1	Background Sources . . . . .	53
111	12.2	Prediction Method . . . . .	53
112	12.3	Validation and Uncertainty . . . . .	53
113	13	SYSTEMATIC UNCERTAINTIES AND RESULTS	55
114	13.1	Systematic Uncertainties . . . . .	55
115	13.2	Final Yields . . . . .	55
116	14	INTERPRETATION	57
117	14.1	Cross Sectional Limits . . . . .	57
118	14.2	Mass Limits . . . . .	57
119	14.3	Context for Long-Lived Searches . . . . .	57
120	VI	CONCLUSIONS	59
121	15	SUMMARY AND OUTLOOK	61
122	15.1	Summary . . . . .	61
123	15.2	Outlook . . . . .	61
124	VII	APPENDIX	63
125	A	INELASTIC CROSS SECTION	65
126	B	APPENDIX TEST	67
127	B.1	Appendix Section Test . . . . .	67
128	B.1.1	Appendix Subection Test . . . . .	67
129	B.2	A Table and Listing . . . . .	67
130	B.3	Some Formulas . . . . .	68
131		BIBLIOGRAPHY	71

132 LIST OF FIGURES

---

133	Figure 1	The particle content of the Standard Model. . . . .	8
134	Figure 2	An illustration (a) of the $E/p$ variable used throughout this paper. The red energy deposits come from the charged particle targeted for measurement, while the blue energy deposits are from nearby neutral particles and must be subtracted. The same diagram (b) for the neutral-background selection, described in Section 8.2.3.	25
135			
136			
137			
138			
139			
140	Figure 3	The $E/p$ distribution and ratio of simulation to data for isolated tracks with (a) $ \eta  < 0.6$ and $1.2 < p/\text{GeV} < 1.8$ and (b) $ \eta  < 0.6$ and $2.2 < p/\text{GeV} < 2.8$ . . . . .	26
141			
142			
143	Figure 4	The fraction of tracks as a function (a, b) of momentum, (c, d) of interaction lengths with $E \leq 0$ for tracks with positive (on the left) and negative (on the right) charge. . . . .	27
144			
145			
146			
147	Figure 5	$\langle E/p \rangle_{\text{BG}}$ as a function of the track momentum for tracks with (a) $ \eta  < 0.6$ , (b) $0.6 <  \eta  < 1.1$ , and as a function of the track pseudorapidity for tracks with (c) $1.2 < p/\text{GeV} < 1.8$ , (d) $1.8 < p/\text{GeV} < 2.2$ . . . . .	29
148			
149			
150			
151	Figure 6	$\langle E/p \rangle_{\text{COR}}$ as a function of track momentum, for tracks with (a) $ \eta  < 0.6$ , (b) $0.6 <  \eta  < 1.1$ , (c) $1.8 <  \eta  < 1.9$ , and (d) $1.9 <  \eta  < 2.3$ . . . . .	30
152			
153			
154	Figure 7	$\langle E/p \rangle_{\text{COR}}$ calculated using LCW-calibrated topological clusters as a function of track momentum for tracks with (a) zero or more associated topological clusters or (b) one or more associated topological clusters. . . . .	31
155			
156			
157			
158	Figure 8	Comparison of the $\langle E/p \rangle_{\text{COR}}$ for tracks with (a) less than and (b) greater than 20 hits in the TRT. . . . .	32
159			
160	Figure 9	Comparison of the $\langle E/p \rangle_{\text{COR}}$ for (a) positive and (b) negative tracks as a function of track momentum for tracks with $ \eta  < 0.6$ . . . . .	32
161			
162			
163	Figure 10	Comparison of the $E/p$ distributions for (a) positive and (b) negative tracks with $0.8 < p/\text{GeV} < 1.2$ and $ \eta  < 0.6$ , in simulation with the FTFP_BERT and QGSP_BERT physics lists. . . . .	33
164			
165			
166			
167	Figure 11	Comparison of the response of the hadronic calorimeter as a function of track momentum (a) at the EM-scale and (b) after the LCW calibration. . . . .	33
168			
169			
170	Figure 12	Comparison of the response of the EM calorimeter as a function of track momentum (a) at the EM-scale and (b) with the LCW calibration. . . . .	34
171			
172			

173	Figure 13	The reconstructed mass peaks of (a) $K_S^0$ , (b) $\Lambda$ , and (c) $\bar{\Lambda}$ candidates. . . . .	35
174			
175	Figure 14	The $E/p$ distribution for isolated (a) $\pi^+$ , (b) $\pi^-$ , (c) proton, and (d) anti-proton tracks. . . . .	36
176			
177	Figure 15	The fraction of tracks with $E \leq 0$ for identified (a) $\pi^+$ and $\pi^-$ , and (b) proton and anti-proton tracks . . . . .	36
178			
179	Figure 16	The difference in $\langle E/p \rangle$ between (a) $\pi^+$ and $\pi^-$ (b) $p$ and $\pi^+$ , and (c) $\bar{p}$ and $\pi^-$ . . . . .	37
180			
181	Figure 17	$\langle E/p \rangle_{\text{COR}}$ as a function of track momentum for (a) $\pi^+$ tracks and (b) $\pi^-$ tracks. . . . .	38
182			
183	Figure 18	The ratio of the calorimeter response to single parti- cles of various species to the calorimeter response to $\pi^+$ with the physics list FTFP_BERT. . . . .	38
184			
185	Figure 19	The spectra of true particles inside anti- $k_t$ , $R = 0.4$ jets with (a) $90 < p_T/\text{GeV} < 100$ , (b) $400 < p_T/\text{GeV} <$ $500$ , and (c) $1800 < p_T/\text{GeV} < 2300$ . . . . .	42
186			
187	Figure 20	The jet energy scale uncertainty contributions, as well as the total jet energy scale uncertainty, as a function of jet $p_T$ for (a) $ \eta  < 0.6$ and (b) $0.6 <  \eta  < 1.1$ . . . . .	44
188			
189	Figure 21	The jet energy scale correlations as a function of jet $p_T$ and $ \eta $ for jets in the central region of the detector. . . . .	45
190			
191			
192			
193			

<sup>194</sup> LIST OF TABLES

---

<sup>195</sup> Table 1	Autem usu id . . . . .	67
------------------------	------------------------	----

<sup>196</sup> LISTINGS

---

<sup>197</sup> Listing 1	A floating example ( <code>listings</code> manual)	68
--------------------------	--	----

198 ACRONYMS

---

199 EG Example

200

## PART I

201

### INTRODUCTION

202

You can put some informational part preamble text here.



# 1

203

204 INTRODUCTION

---



205

## PART II

206

### THEORETICAL CONTEXT

207

You can put some informational part preamble text here.



# 2

208

## 209 STANDARD MODEL

---

210 The Standard Model of particle physics seeks to explain the symmetries and in-  
211 teractions of all currently discovered fundamental particles. It has been tested by  
212 several generations of experiments and has been remarkably successful, no sig-  
213 nificant deviations have been found. The Standard Model provides predictions  
214 in particle physics for interactions up to the Planck scale ( $10^{15}$ - $10^{19}$  GeV).

215 The theory itself is a quantum field theory grown from an underlying  $SU(3) \times$   
216  $SU(2) \times U(1)$  that requires the particle content and quantum numbers consist-  
217 ent with experimental observations (see Section 2.1). Each postulated symme-  
218 try is accompanied by an interaction between particles through gauge invari-  
219 ance. These interactions are referred to as the Strong, Weak, and Electromag-  
220 netic forces, which are discussed in Section 2.2.

221 Although this model has been very predictive, the theory is incomplete; for  
222 example, it is not able to describe gravity or astronomically observed dark matter.  
223 These limitations are discussed in more detail in Section 2.3.

## 224 21 PARTICLES

225 The most familiar matter in the universe is made up of protons, neutrons, and  
226 electrons. Protons and neutrons are composite particles, however, and are made  
227 up in turn by particles called quarks. Quarks carry both electric charge and color  
228 charge, and are bound in color-neutral combinations called baryons. The elec-  
229 tron is an example of a lepton, and carries only electric charge. Another type  
230 of particle, the neutrino, does not form atomic structures in the same way that  
231 quarks and leptons do because it carries no color or electric charge. Collectively,  
232 these types of particles are known as fermions, the group of particles with half-  
233 integer spin.

234 There are three generations of fermions, although familiar matter is formed  
235 predominantly by the first generation. The generations are identical except for  
236 their masses, which increase in each generation by convention. In addition, each  
237 of these particles is accompanied by an antiparticle, with opposite-sign quantum  
238 numbers but the same mass.

239 The fermions comprise what is typically considered matter, but there are  
240 additional particles that are mediators of interactions between those fermions.  
241 These mediators are known as the gauge bosons, gauge in that their existence  
242 is required by gauge invariance (discussed further in Section 2.2) and bosons in  
243 that they have integer spin. The boson which mediates the electromagnetic force  
244 is the photon, the first boson to be discovered; it has no electric charge, no mass,  
245 and a spin of 1. There are three spin-1 mediators of the weak force, the two W  
246 bosons and the Z boson. The W bosons have electric charge of  $\pm 1$  and a mass of  
247  $80.385 \pm 0.015$  GeV, while the Z boson is neutral and has a mass of  $91.1876 \pm$

248 0.0021 GeV. The strong force is mediated by eight particles called gluons, which  
 249 are massless and electrically neutral but do carry color charge.

250 The final particle present in the Standard Model is the Higgs boson, which was  
 251 recently observed for the first time by experiments at CERN in 2012. It is electro-  
 252 cally neutral, has a mass of  $125.7 \pm 0.4$  GeV, and is the only spin-0 particle yet to  
 253 be observed. The Higgs boson is the gauge boson associated with the mechanism  
 254 that gives a mass to the W and Z bosons.

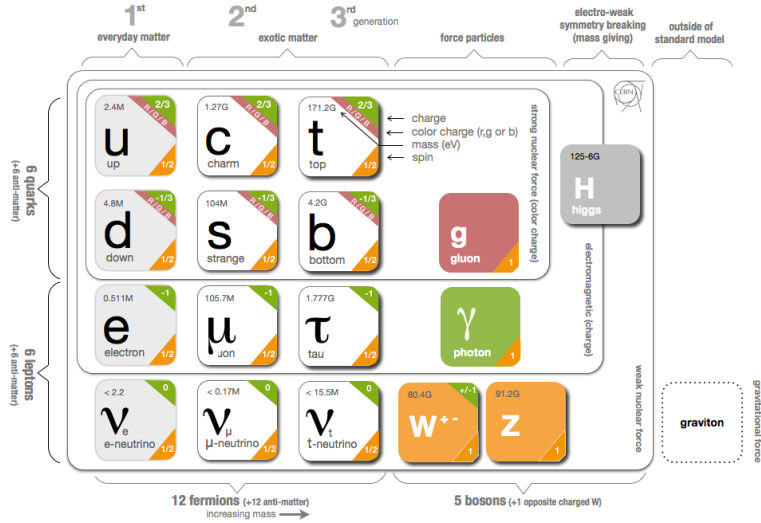


Figure 1: The particle content of the Standard Model.

255 Together these particles form the entire content of the Standard Model, and  
 256 are summarized in Figure 1. These are the particles that constitute the observable  
 257 universe and all the so-far-observed interactions within it.

## 258 2.2 INTERACTIONS

259 The interactions predicted and described by the Standard Model are fundamen-  
 260 tally tied to the particles within it, both in that they describe the way those par-  
 261 ticles can influence each other and also in that the existence of the interactions  
 262 requires the existence of some particles (the gauge bosons).

## 263 2.3 LIMITATIONS

# 3

264

265 SUPERSYMMETRY

---

266 3.1 MOTIVATION

267 3.2 STRUCTURE

268 3.3 PHENOMENOLOGY



# 4

269

270 LONG-LIVED PARTICLES

---

271 4.1 MECHANISMS

272 4.1.1 EXAMPLES IN SUPERSYMMETRY

273 4.2 PHENOMENOLOGY

274 4.2.1 DISIMILARITIES TO PROMPT DECAYS

275 4.2.2 CHARACTERISTIC SIGNATURES



276

### PART III

277

## EXPERIMENTAL STRUCTURE AND RECONSTRUCTION

278

You can put some informational part preamble text here.



# 5

279

280 THE LARGE HADRON COLLIDER

---

281 5.1 INJECTION CHAIN

282 5.2 DESIGN AND PARAMETERS

283 5.3 LUMINOSITY



# 6

284

## 285 THE ATLAS DETECTOR

---

286 6.1 COORDINATE SYSTEM

287 6.2 MAGNETIC FIELD

288 6.3 INNER DETECTOR

289 6.3.1 PIXEL DETECTOR

290 6.3.2 SEMICONDUCTOR TRACKER

291 6.3.3 TRANSITION RADIATION TRACKER

292 6.4 CALORIMETRY

293 6.4.1 ELECTROMAGNETIC CALORIMETERS

294 6.4.2 HADRONIC CALORIMETERS

295 6.4.3 FORWARD CALORIMETERS

296 6.5 MUON SPECTROMETER

297 6.6 TRIGGER

298 6.6.1 TRIGGER SCHEME

299 6.6.2 MISSING TRANSVERSE ENERGY TRIGGERS



# 7

300

## 301 EVENT RECONSTRUCTION

---

302 The ATLAS experiment combines measurements in the subdetectors to form a  
303 cohesive picture of each physics event.

## 304 7.1 TRACKS AND VERTICES

### 305 7.1.1 TRACK RECONSTRUCTION

#### 306 7.1.1.1 NEURAL NETWORK

#### 307 7.1.1.2 PIXEL DE/DX

#### 308 7.1.2 VERTEX RECONSTRUCTION

## 309 7.2 JETS

### 310 7.2.1 TOPOLOGICAL CLUSTERING

### 311 7.2.2 JET ENERGY SCALE

### 312 7.2.3 JET ENERGY SCALE UNCERTAINTIES

### 313 7.2.4 JET ENERGY RESOLUTION

## 314 7.3 ELECTRONS

### 315 7.3.1 ELECTRON IDENTIFICATION

## 316 7.4 MUONS

### 317 7.4.1 MUON IDENTIFICATION

## 318 7.5 MISSING TRANSVERSE ENERGY



319

## PART IV

320

### CALORIMETER RESPONSE

321

You can put some informational part preamble text here.



322

323 RESPONSE MEASUREMENT WITH SINGLE HADRONS

---

324 As discussed in Section 7.2, colored particles produced in collisions hadronize  
325 into jets of multiple individual hadrons. One approach to understanding jet physics  
326 in the ATLAS calorimetry is to evaluate the calorimeter response to those indi-  
327 vidual hadrons; measurements of individual hadrons can be used to build up  
328 an understanding of the jets that they form. The redundancy of the momentum  
329 provided by the tracking system and the energy provided by the calorimeter pro-  
330 vides an opportunity to study calorimeter response using real collisions, as de-  
331 scribed further in Section 8.2.

332 A number of interesting factors compromise calorimeter response, and ex-  
333 tracting these separately provides insight into many aspects of jet modeling. First,  
334 many charged hadrons interact with the material of the detector prior to reach-  
335 ing the calorimeters and thus do not deposit any energy. Comparing this effect in  
336 data and simulation is a powerful tool in validating the interactions of particles  
337 with the material of the detector as well as the model of the detector geometry  
338 in simulation, see Section 8.2.2. The particles which do reach the calorimeter de-  
339 posit their energy into individual cells, which are then clustered to measure full  
340 energy deposits. Comparing the response in data to simulated hadrons provides  
341 a direct evaluation of several aspects of simulation: noise in the calorimeters, the  
342 showering of hadronic particles, and the energy deposited by particles in mat-  
343 ter, among others (Section 8.2.4). These measurements are extended to explore  
344 several additional effects, such as the dependence on charge, in Section 8.2.4.1.

345 The above studies all use an inclusive selection of charged particles, which are  
346 compromised predominantly of pions, kaons, and (anti)protons. It is also inter-  
347 esting to measure the particle types separately to evaluate the simulated inter-  
348 actions of each particle, particularly at low energies where differences between  
349 species are very relevant. Pions and (anti)protons can be identified through de-  
350 cays of long-lived particles, in particular  $\Lambda$ ,  $\bar{\Lambda}$ , and  $K_S^0$ , and then used to measure  
351 response as described above. This is discussed in detail in Section 8.3.

352 Together, these measurements in data provide a thorough understanding of  
353 the way hadrons interact with the ATLAS detector and can be used to build up a  
354 description of jets, as seen in Chapter 9. The results in this chapter use data col-  
355 lected at 7 and 8 TeV collected in 2010 and 2012, respectively. Both are included  
356 as the calorimeter was repaired and recalibrated between those two data-taking  
357 periods. Both sets of data are compared to an updated simulation that includes  
358 new physics models provided by Geant4 [12] and improvements in the detector  
359 description [2, 6]. These results are published in EPJC [8] and can be compared to  
360 a similar measurement performed in 2009 and 2010 [5], which used the previous  
361 version of the simulation framework [1].

## 362 8.1 DATASET AND SIMULATION

## 363 8.1.1 DATA SAMPLES

364 The two datasets used in this chapter are taken from dedicated low-pileup runs  
 365 where the fraction of events with multiple interactions was negligible, to facilitate  
 366 measurement of isolated hadrons. The 2012 dataset at  $\sqrt{s} = 8$  TeV contains  
 367 8 million events and corresponds to an integrated luminosity of  $0.1 \text{ nb}^{-1}$ . The  
 368 2010 dataset at  $\sqrt{s} = 7$  TeV contains 3 million events and corresponds to an  
 369 integrated luminosity of  $3.2 \text{ nb}^{-1}$ . This last dataset was also used in the 2010 re-  
 370 sults [5], but it has since been reanalyzed with an updated detector description  
 371 for the material and alignment.

## 372 8.1.2 SIMULATED SAMPLES

373 The two datasets above are compared to simulated single-, double-, and non-  
 374 diffractive events generated with Pythia8 [32] using the A2 configuration of  
 375 hadronization [3] and the MSTW 2008 parton-distribution function set [28, 31].  
 376 The conditions and energies for each run are matched in the two simulations.

377 To evaluate the interaction of hadrons with detector material, the simulation  
 378 uses two different collections of hadronic physics models, called physics lists, in  
 379 Geant4 9.4 [30]. The first, QGSP\_BERT, combines the Bertini intra-nuclear  
 380 cascade [17, 24, 26] below 9.9 GeV, a parametrized proton inelastic model from  
 381 9.5 to 25 GeV [21], and a quark-gluon string model above 12 GeV [13, 14, 18, 19,  
 382 22]. The second, FTFP\_BERT, combines the Bertini intra-nuclear cascade [17, 24,  
 383 26] below 5 GeV and the Fritiof model [15, 16, 23, 29] above 4 GeV. In either list,  
 384 Geant4 enforces a smooth transition between models where multiple models  
 385 overlap.

## 386 8.1.3 EVENT SELECTION

387 The event selection for this study is minimal, as the only requirement is selecting  
 388 good-quality events with an isolated track. Such events are triggered by requir-  
 389 ing at least two hits in the minimum-bias trigger scintillators. After trigger, each  
 390 event is required to have exactly one reconstructed vertex, and that vertex is re-  
 391 quired to have four or more associated tracks.

392 The particles which enter into the response measurements are first identified  
 393 as tracks in the inner detector. To ensure a reliable momentum measurement,  
 394 these tracks are required to have at least one hit in the pixel detector, six hits in  
 395 the SCT, and small longitudinal and transverse impact parameters with respect  
 396 to the primary vertex [5]. For the majority of the measurements in this chap-  
 397 ter, the track is additionally required to have 20 hits in the TRT, which signifi-  
 398 cantly reduces the contribution from tracks which undergo nuclear interactions.  
 399 This requirement and its effect is discussed in more detail in Section 8.2.4.1. In  
 400 addition, tracks are rejected if there is another track which extrapolates to the  
 401 calorimeter within a cone of  $\Delta R = \sqrt{(\Delta\phi)^2 + (\Delta\eta)^2} < 0.4$ . This requirement

402 guarantees that the contamination of energy from nearby charged particles is  
 403 negligible [5].

## 404 8.2 INCLUSIVE HADRON RESPONSE

405 The calorimeter response is more precisely defined as the ratio of the measured  
 406 calorimeter energy to the true energy carried by the particle, although this true  
 407 energy is unknown. For charged particles, however, the inner detector provides  
 408 a very precise measurement of momentum (with uncertainty less than 1%) that  
 409 can be used as a proxy for true energy. The ratio of the energy deposited by the  
 410 charged particle in the calorimeter,  $E$ , to its momentum measured in the inner  
 411 detector  $p$ , forms the calorimeter response measure called  $E/p$ . Though the dis-  
 412 tribution of  $E/p$  is interesting, two aggregated quantities are more directly use-  
 413 ful:  $\langle E/p \rangle$ , the average of  $E/p$  within a given subset of particles, and the zero  
 414 fraction, the fraction of particles with no associated energy in the calorimeter.

415 The calorimeter energy assigned to a track particle is defined using clusters.  
 416 The clusters are formed using a 4–2–0 algorithm [9] that begins with seeds re-  
 417 quiring at least 4 times the average calorimeter noise. The neighboring cells with  
 418 at least twice that noise threshold are then added to the cluster, and all bound-  
 419 ing cells are then added with no requirement. This algorithm minimizes noise  
 420 contributions through its seeding process, and including the additional layers  
 421 improves the energy resolution [33]. The clusters are associated to a given track  
 422 if they fall within a cone of  $\Delta R = 0.2$  of the extrapolated position of the track,  
 423 which includes about 90% of the energy on average [5]. This construction is il-  
 424 lustrated in Figure 2.

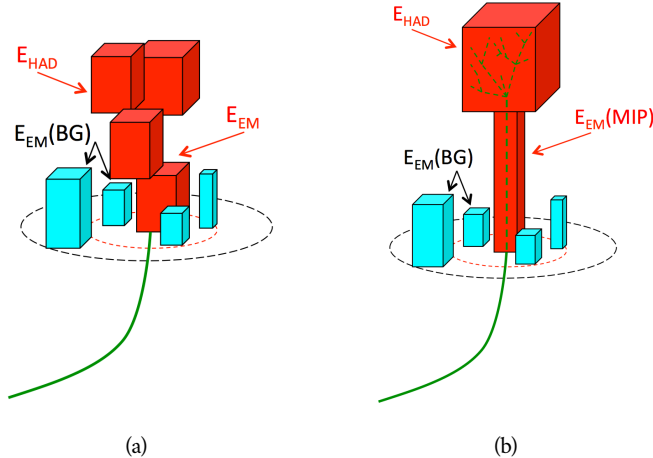


Figure 2: An illustration (a) of the  $E/p$  variable used throughout this paper. The red energy deposits come from the charged particle targeted for measurement, while the blue energy deposits are from nearby neutral particles and must be subtracted. The same diagram (b) for the neutral-background selection, described in Section 8.2.3.

## 425 8.2.1 E/P DISTRIBUTION

426 The  $E/p$  distributions measured in both data and simulation are shown in Figure 3 for two example bins of track momentum and for tracks in the central  
 427 region of the detector. These distributions show several important features of  
 428 the  $E/p$  observable. The large content in the bin at  $E = 0$  comes from tracks that  
 429 have no associated cluster, which occurs due to interactions with detector mate-  
 430 rial prior to reaching the calorimeter or the energy deposit being insufficiently  
 431 large to generate a seed, and are discussed in Section 8.2.2. The small negative  
 432 tail comes from similar tracks that do not deposit any energy in the calorimeter  
 433 but are randomly associated to a noise cluster. The long positive tail above 1.0  
 434 comes from the contribution of neutral particles. Nearby neutral particles de-  
 435 posit (sometimes large) additional energy in the calorimeter but do not produce  
 436 tracks in the inner detector, so they cannot be rejected for isolation. Additionally  
 437 the peak and mean of the distribution falls below 1.0 because of the loss of energy  
 438 not found within the cone as well as the non-compensation of the calorimeter.  
 439

440 The data and simulation share the same features, but the high and low tails  
 441 are significantly different. The simulated events tend to overestimate the contri-  
 442 bution of neutral particles to the long tail, an effect which can be isolated and  
 443 removed as discussed in Section 8.2.3. Additionally, the simulated clusters have  
 444 less noise on average, although this is a small effect on the overall response.

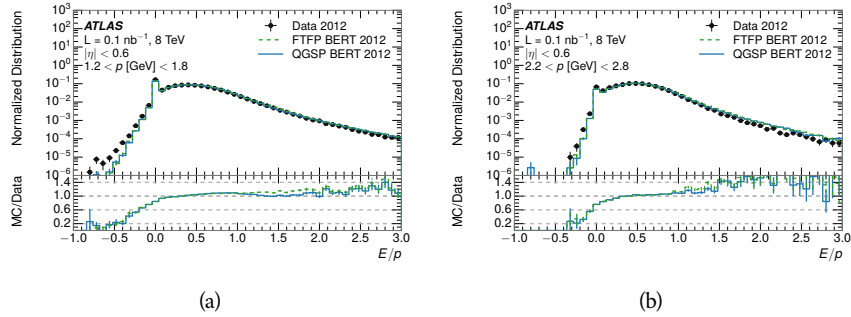


Figure 3: The  $E/p$  distribution and ratio of simulation to data for isolated tracks with  
 (a)  $|\eta| < 0.6$  and  $1.2 < p/\text{GeV} < 1.8$  and (b)  $|\eta| < 0.6$  and  $2.2 < p/\text{GeV} < 2.8$ .

## 445 8.2.2 ZERO FRACTION

446 The fraction of particles with no associated clusters, or similarly those with  $E \leq$   
 447 0, reflects the modeling of both the detector geometry and hadronic interactions.  
 448 The zero fraction is expected to rise as the amount of material a particle traverses  
 449 increases, while it is expected to decrease as the particle energy increases. This  
 450 dependence can be seen in Figure 4, where the zero fraction in data and simula-  
 451 tion is shown as a function of momentum and the amount of material measured  
 452 in interaction lengths. The trends are similar between the 2010 and 2012 mea-  
 453 surements. The zero fraction decreases with energy as expected. The amount of  
 454 material in the detector increases with  $\eta$ , which provides a distribution of inter-

action lengths. As the data and simulation have significant disagreement in the zero fraction over a number of interaction lengths, the difference must be primarily from the modeling of hadronic interactions with detector material and not just the detector geometry.

There is also a noticeable difference between positive and negative tracks at low momentum, which reflects the difference in response between protons and antiprotons. Antiprotons have significant model differences in the two physics lists, QGSP\_BERT and FTFP\_BERT, and this is evident in the lowest momentum bin of the data to simulation ratio. This difference is explored further in Section 8.3.

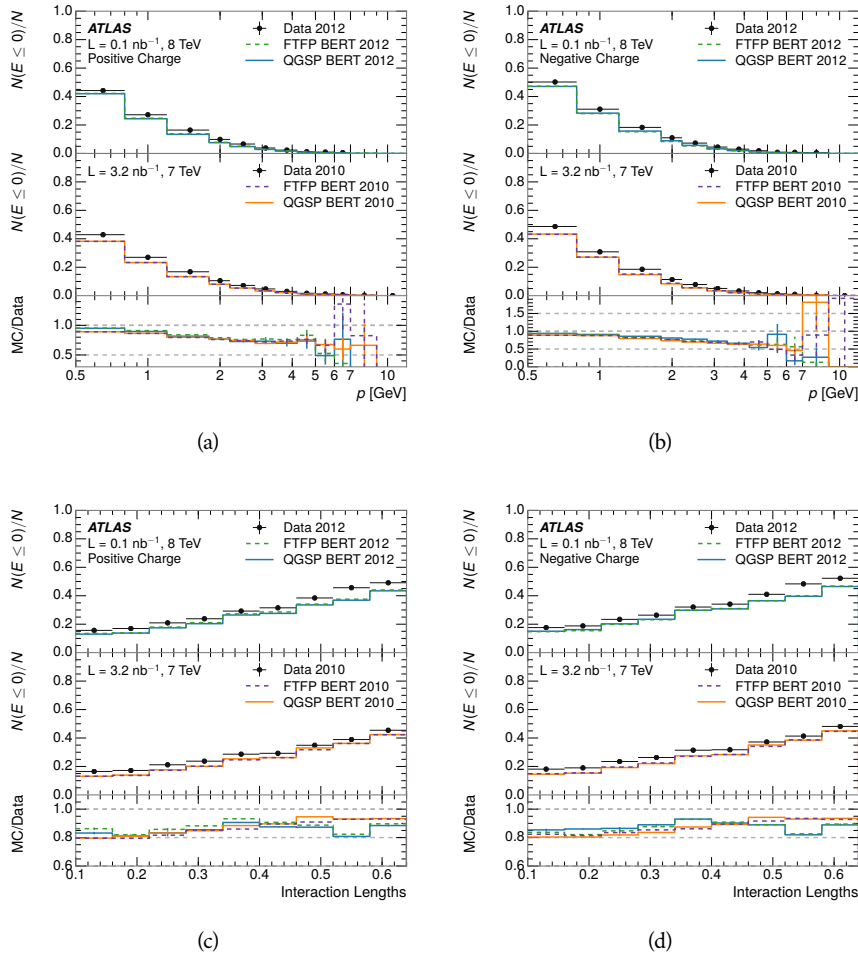


Figure 4: The fraction of tracks as a function (a, b) of momentum, (c, d) of interaction lengths with  $E \leq 0$  for tracks with positive (on the left) and negative (on the right) charge.

### 8.2.3 NEUTRAL BACKGROUND SUBTRACTION

The isolation requirement on hadrons is only effective in remove energy contribution from nearby charged particles. Nearby neutral particles, predominantly

468 photons from  $\pi^0$  decays, also add their energy to the calorimeter clusters, but  
 469 mostly in the electromagnetic calorimeter. It is possible to measure this contribu-  
 470 tion, on average, using late-showering hadrons that minimally ionize in the  
 471 electromagnetic calorimeter. Such particles are selected by requiring that they  
 472 deposit less than 1.1 GeV in the EM calorimeter within a cone of  $\Delta R < 0.1$   
 473 around the track. To ensure that these particles are well measured, they are addi-  
 474 tionally required to deposit between 40% and 90% of their energy in the hadronic  
 475 calorimeter within the same cone.

476 These particles provide a clean sample to measure the nearby neutral back-  
 477 ground because they do not deposit energy in the area immediately surrounding  
 478 them in the EM calorimeter, as shown in Figure 2. So, the energy deposits in the  
 479 region  $0.1 < \Delta R < 0.2$  can be attributed to neutral particles alone. To estimate  
 480 the contribution to the whole cone considered for the response measurement,  
 481 that energy is scaled by a geometric factor of 4/3. This quantity,  $\langle E/p \rangle_{\text{BG}}$ , mea-  
 482 sured in aggregate over a number of particles, gives the contribution to  $\langle E/p \rangle$   
 483 from neutral particles in the EM calorimeter. Similar techniques were used in  
 484 the individual layers of the hadronic calorimeters to show that the background  
 485 from neutrals is negligible in those layers [5].

486 The distribution of this background estimate is shown in Figure 5. Although  
 487 the simulation captures the overall trend, it significantly overestimates the neu-  
 488 tral contribution for tracks with momentum between 2 and 8 GeV. This effect  
 489 was also seen in the tails of the  $E/p$  distributions in Figure 3. This difference is  
 490 likely due to the modeling of coherent neutral particle radiation in Pythia8, as  
 491 the discrepancy does not depend on  $\eta$  and thus is unlikely to be a mismodeling  
 492 of the detector. This difference can be subtracted to form a corrected average  
 493  $E/p$ , as in Section 8.2.4.

#### 494 8.2.4 CORRECTED RESPONSE

495 Figure 6 shows  $\langle E/p \rangle_{\text{COR}}$  as a function of momentum for several bins of pseu-  
 496 dorapidity. This corrected  $\langle E/p \rangle_{\text{COR}} \equiv \langle E/p \rangle - \langle E/p \rangle_{\text{BG}}$  measures the average  
 497 calorimeter response without the contamination of neutral particles. It is the  
 498 most direct measurement of calorimeter response in that it is the energy mea-  
 499 sured for fully isolated hadrons. The correction is performed separately in data  
 500 and simulation, so that the mismodeling of the neutral background in simulation  
 501 is removed from the comparison of response. The simulation overestimates the  
 502 response at low momentum by about 5%, an effect that can be mostly attributed  
 503 to the underestimation of the zero fraction mentioned previously.

504 The response measurement above used topological clustering at the EM scale,  
 505 that is clusters were formed to measure energy but no corrections were applied  
 506 to correct for expected effects like energy lost outside of the cluster or in unin-  
 507 strumented material. It is also interesting to measure  $\langle E/p \rangle_{\text{COR}}$  using local clus-  
 508 ter weighted (LCW) energies, which accounts for those effects by calibrating the  
 509 energy based on the properties of the cluster such as energy density and depth  
 510 in the calorimeter. Figure 7 shows these distributions for tracks with zero or  
 511 more clusters and separately for tracks with one or more clusters. The calibra-

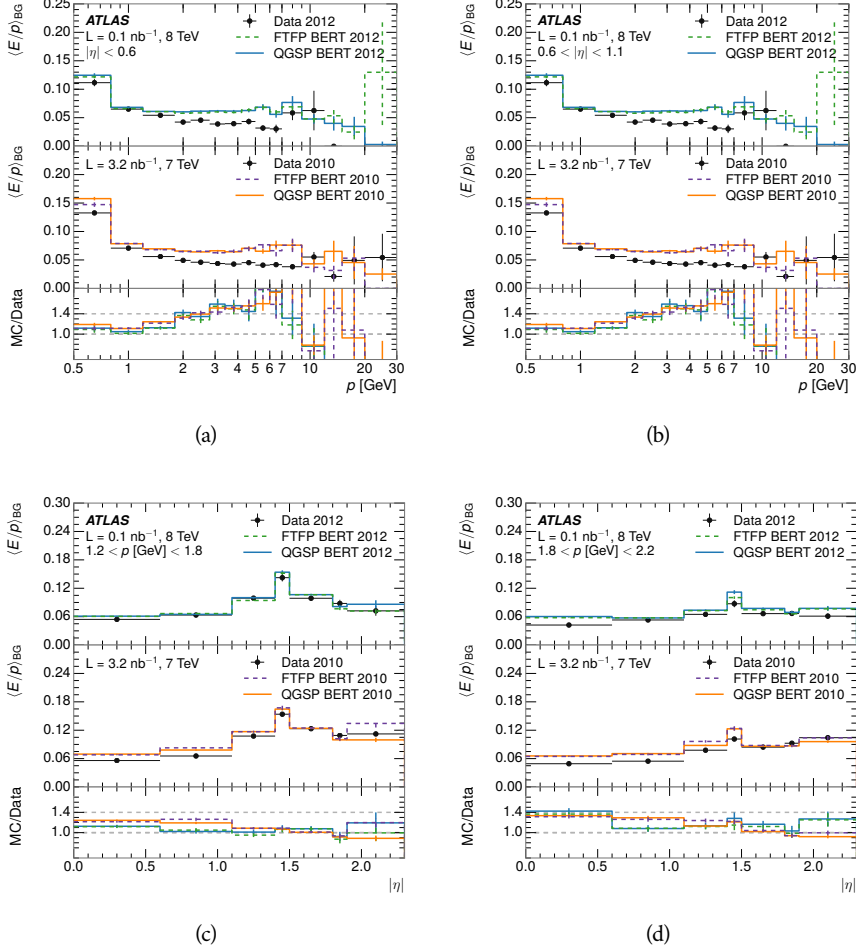


Figure 5:  $\langle E/p \rangle_{BG}$  as a function of the track momentum for tracks with (a)  $|\eta| < 0.6$ , (b)  $0.6 < |\eta| < 1.1$ , and as a function of the track pseudorapidity for tracks with (c)  $1.2 < p/\text{GeV} < 1.8$ , (d)  $1.8 < p/\text{GeV} < 2.2$ .

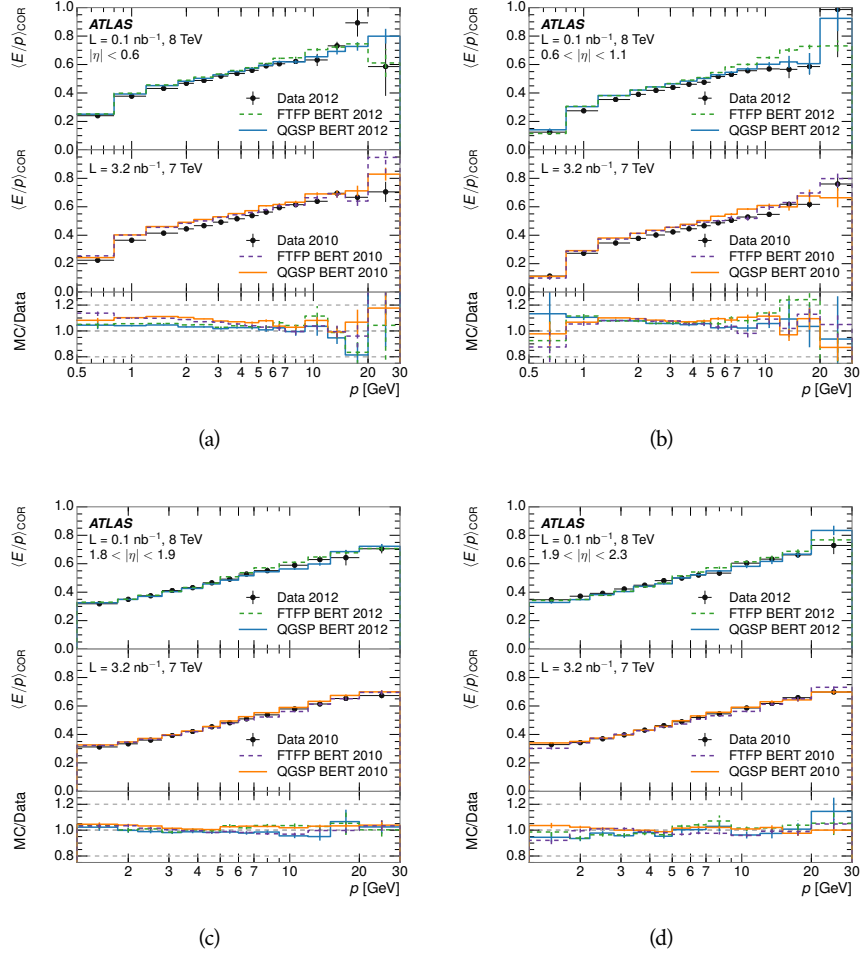


Figure 6:  $\langle E/p \rangle_{\text{COR}}$  as a function of track momentum, for tracks with (a)  $|\eta| < 0.6$ , (b)  $0.6 < |\eta| < 1.1$ , (c)  $1.8 < |\eta| < 1.9$ , and (d)  $1.9 < |\eta| < 2.3$ .

tion moves  $\langle E/p \rangle_{\text{COR}}$  significantly closer to 1.0, which is the purpose of the calibration. The agreement between data and simulation improves noticeably when at least one cluster is required, as this removes the contribution from the mismodeling of zero fraction.

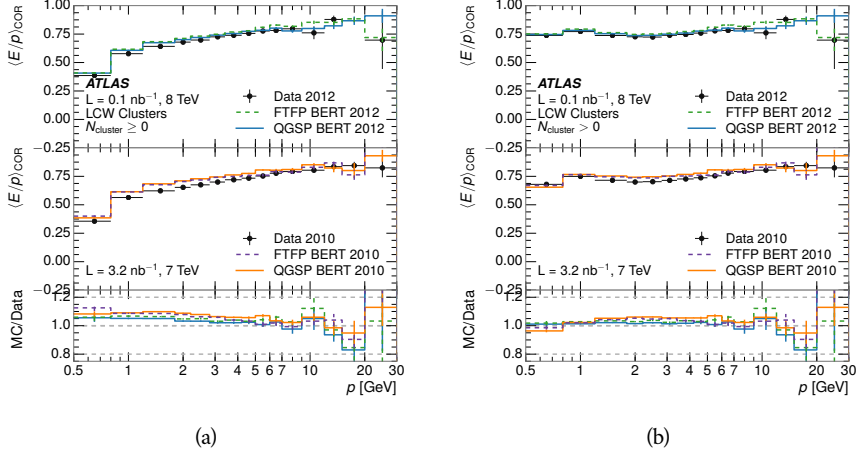


Figure 7:  $\langle E/p \rangle_{\text{COR}}$  calculated using LCW-calibrated topological clusters as a function of track momentum for tracks with (a) zero or more associated topological clusters or (b) one or more associated topological clusters.

#### 8.2.4.1 ADDITIONAL STUDIES

As has been seen in several previous measurements, the simulation does not correctly model the chance of a low momentum hadron to reach the calorimeter. Because of the consistent discrepancy across pseudorapidity and interaction lengths, this seems to be best explained by incomplete understanding of hadronic interactions with the detector. For example, a hadron that scatters off of a nucleus in the inner detector can be deflected through a significant angle and not reach the expected location in the calorimeter. In addition, these interaction can produce secondary particles that are difficult to model.

The requirement on the number of hits in the TRT reduces these effects by preferentially selecting tracks that do not undergo nuclear interactions. It is interesting to check how well the simulation models tracks with low numbers of TRT hits, where the nuclear interactions are much more likely. Figure 8 compares the distributions with  $N_{\text{TRT}} < 20$  to  $N_{\text{TRT}} > 20$  for real and simulated particles. As expected, the tracks with fewer hits are poorly modeled in the simulation as  $\langle E/p \rangle_{\text{COR}}$  differs by as much as 25% at low momentum.

Another interesting aspect of the simulation is the description of antiprotons at low momentum, where QGSP\_BERT and FTFP\_BERT have significant differences. This can be seen to have an effect in the inclusive response measurement when separated into positive and negative charge. The  $\langle E/p \rangle_{\text{COR}}$  distributions for positive and negative particles are shown in Figure 9, where a small difference between QGSP\_BERT and FTFP\_BERT can be seen in the distribution for negative tracks. This is demonstrated more clearly in Figure 10, which shows

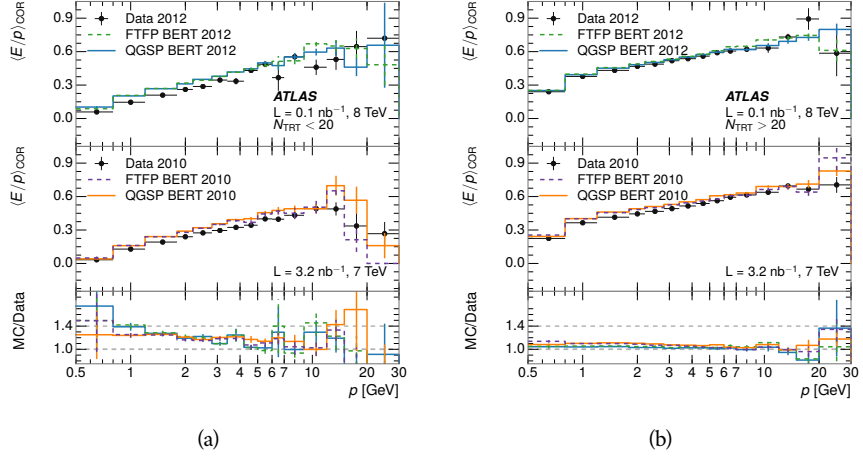


Figure 8: Comparison of the  $\langle E/p \rangle_{\text{COR}}$  for tracks with (a) less than and (b) greater than 20 hits in the TRT.

the  $E/p$  distribution in the two simulations separated by charge. There is a clear difference around  $E/p > 1.0$ , which can be explained by the additional energy deposited by the annihilation of the antiproton in the calorimeter that is modeled well only in FTFP\_BERT. This is also explored with data using identified antiprotons in Section 8.3.

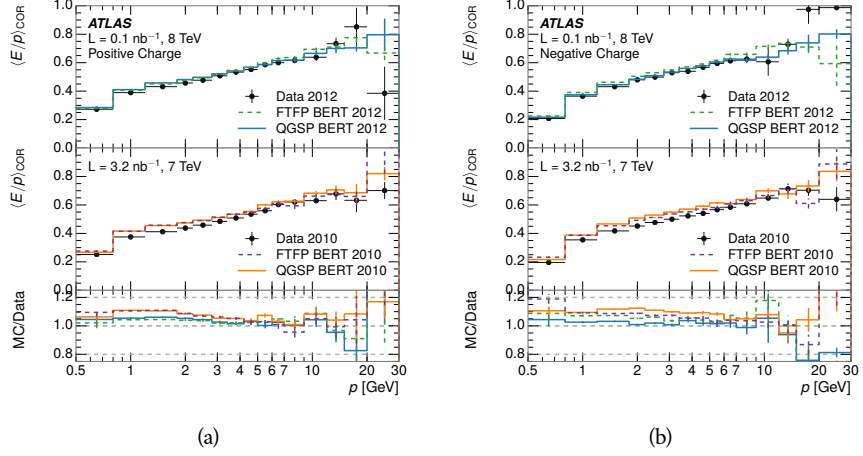


Figure 9: Comparison of the  $\langle E/p \rangle_{\text{COR}}$  for (a) positive and (b) negative tracks as a function of track momentum for tracks with  $|\eta| < 0.6$ .

The  $\langle E/p \rangle$  results in previous sections have considered the electromagnetic and hadronic calorimeters together as a single energy measurement, to emphasize the total energy deposited for a given particle. However, the deposits in each calorimeter are available separately and  $\langle E/p \rangle$  can be constructed for each layer. As the layers are composed of different materials and are modeled separately in the detector geometry, confirm that the simulation matches the data well in each

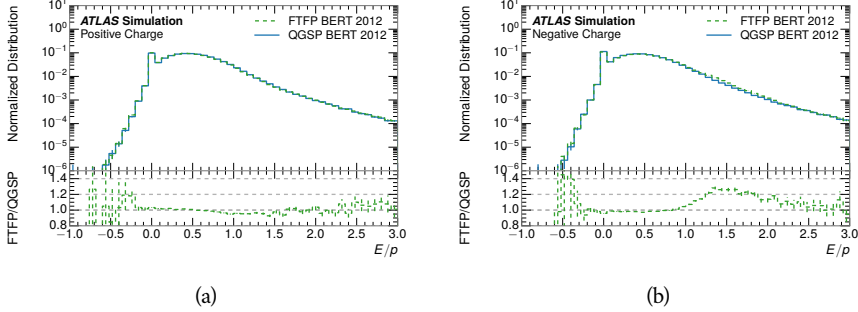


Figure 10: Comparison of the  $E/p$  distributions for (a) positive and (b) negative tracks with  $0.8 < p/\text{GeV} < 1.2$  and  $|\eta| < 0.6$ , in simulation with the FTFP\_BERT and QGSP\_BERT physics lists.

layer adds confidence in both the description of hadronic interactions with the two different materials and also the geometric description of each.

The technique discussed in Section 8.2.3 for selection minimally ionizing particles (MIPs) in the electromagnetic calorimeter is also useful in studying deposits in the hadronic calorimeter. Those MIPs deposit almost all of their energy exclusively in the hadronic calorimeter. Figure 11 shows  $\langle E/p \rangle_{\text{RAW}}^{\text{Had}}$ , where RAW indicates that no correction has been applied for neutral backgrounds and Had indicates that only clusters for the hadronic calorimeter are included. The RAW and COR versions of  $\langle E/p \rangle$  in this case are the same, as the neutral background is negligible in that calorimeter layer. The distributions are shown both for the original EM scale calibration and after LCW calibration. The data and simulation agree very well in this comparison, except in the lowest momentum bin which has 5% discrepancy that has been reflected in similar results.

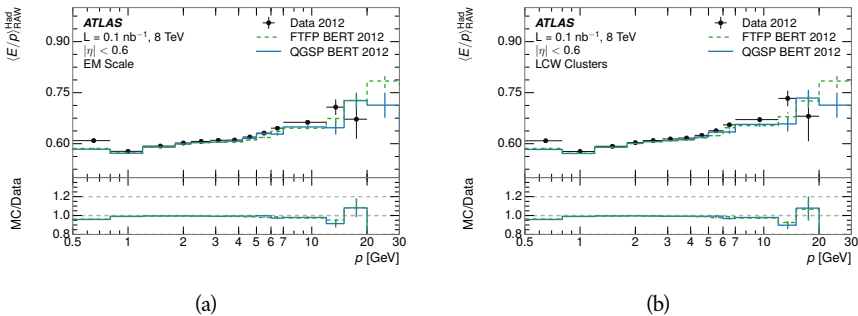


Figure 11: Comparison of the response of the hadronic calorimeter as a function of track momentum (a) at the EM-scale and (b) after the LCW calibration.

A similar comparison can be made in the electromagnetic calorimeter by selecting particles which have no associated energy in the hadronic calorimeter. These results are measured in terms of  $\langle E/p \rangle_{\text{COR}}^{\text{EM}}$ , where EM designates that only clusters in the electromagnetic calorimeter are included and COR designates that the neutral background is subtracted as the neutral background is present in this case. Figure 12 shows the analogous comparisons to Figure 11 in the elec-

tromagnetic calorimeter. In this case the disagreement between data and simulation is more pronounced, with discrepancies as high as 5% over a larger range of momenta. This level of discrepancy indicates that the description of the electromagnetic calorimeter is actually the dominant source of discrepancy in the combined distributions in Section 8.2.4.

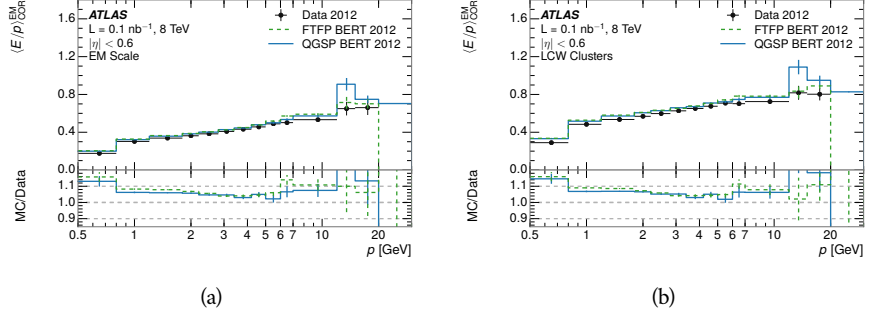


Figure 12: Comparison of the response of the EM calorimeter as a function of track momentum (a) at the EM-scale and (b) with the LCW calibration.

**NOTE: There are more studies that I skipped for brevity that could be included if interesting.  $E/p$  at different cluster threshold settings,  $E/p$  with pileup,  $E/p$  with cells. I also left out a lot of eta bins that appear in the paper so that this section didn't turn into 20 pages of plots.**

### 8.3 IDENTIFIED PARTICLE RESPONSE

The inclusive response measurement for hadrons can be augmented by measuring the response for specific particle species. The simulation models each particle type separately, and understanding the properties of each is important in constraining the uncertainty on jets. In order to select and measure specific hadrons, this section relies on the displaced decays of long-lived particles. Such decays can be identified by reconstructing secondary vertices, and the particles used decay predominantly to specific hadrons. In particular,  $\Lambda$ ,  $\bar{\Lambda}$ , and  $K_S^0$  can be used to select a pure sample of protons, antiprotons, and pions, respectively.

#### 8.3.1 DECAY RECONSTRUCTION

The measurement of response for identified particles uses the same selection as for inclusive particles (Section 8.1.3) with a few additions. Each event used is required to have at least one secondary vertex, and the tracks are required to match to that vertex rather than the primary vertex. Pions are selected from decays of  $K_S^0 \rightarrow \pi^+ \pi^-$ , which is the dominant decay for  $K_S^0$  to charged particles. Protons are selected from decays of  $\Lambda \rightarrow \pi^- p$  and antiprotons from  $\bar{\Lambda} \rightarrow \pi^+ \bar{p}$ , which are similarly the dominant decays of  $\Lambda$  and  $\bar{\Lambda}$  to charged particles. The species of parent hadron in these decays is determined by reconstructing the mass of the tracks associated to the secondary vertex. The sign of the higher

597 momentum decay particle can distinguish between  $\Lambda$  and  $\bar{\Lambda}$ , which of course  
 598 have the same mass, as the proton or antiproton is kinematically favored to have  
 599 higher momentum. Examples of the reconstructed masses used to select these  
 600 decays are shown in Figure 13.

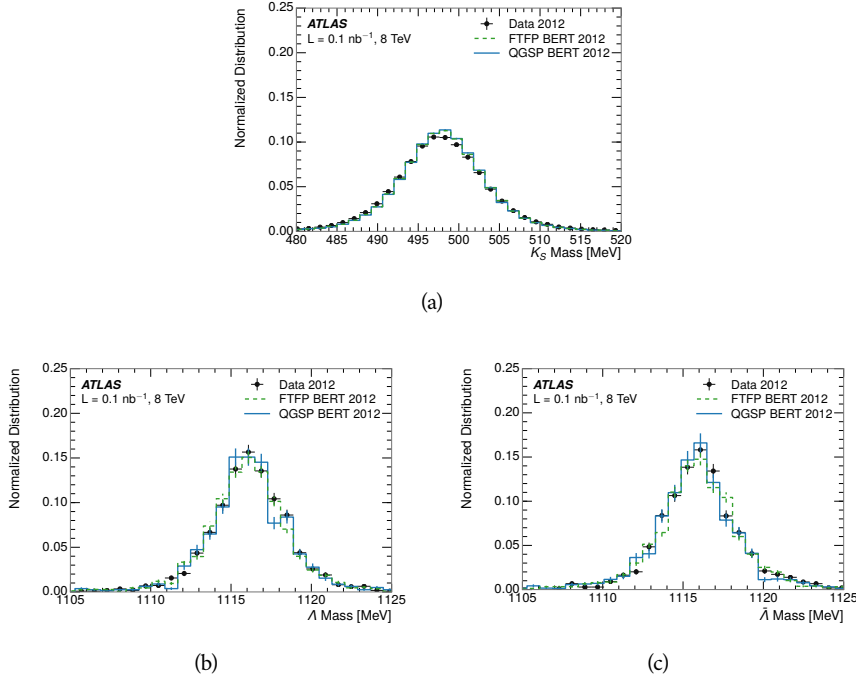


Figure 13: The reconstructed mass peaks of (a)  $K_S^0$ , (b)  $\Lambda$ , and (c)  $\bar{\Lambda}$  candidates.

601 There are a number of sources of backgrounds for these identified particles,  
 602 including nuclear interactions and combinatoric sources. These are suppressed  
 603 by the kinematic requirements on the tracks as well as an additional veto which  
 604 removes candidates that are consistent with both a  $\Lambda$  or  $\bar{\Lambda}$  and a  $K_S^0$  hypothesis,  
 605 which is possible because of the different assumptions on particle mass in each  
 606 case [5]. After these requirements, the backgrounds are found to be negligible  
 607 compared to the statistical errors on these measurements.

### 608 8.3.2 IDENTIFIED RESPONSE

609 With these techniques the  $E/p$  distributions are extracted in data and simulation  
 610 for each particle species and shown in Figure 14. These distributions are shown  
 611 for a particular bin of  $E_a$  ( $2.2 < E_a/\text{GeV} < 2.8$ ), rather than  $p$ .  $E_a$  is the energy  
 612 available to be deposited in the calorimeter: for pions  $E_a = \sqrt{p^2 + m^2}$ , for pro-  
 613 tons  $E_a = \sqrt{p^2 + m^2} - m$ , and for antiprotons  $E_a = \sqrt{p^2 + m^2} + m$ . The features  
 614 of the  $E/p$  distributions are similar to the inclusive case. There is a small nega-  
 615 tive tail from noise and a large fraction of tracks with zero energy from tracks  
 616 which do not reach the calorimeter. The long positive tail is noticeably more  
 617 pronounced for antiprotons because of the additional energy generated by the  
 618 annihilation in addition to the neutral background.

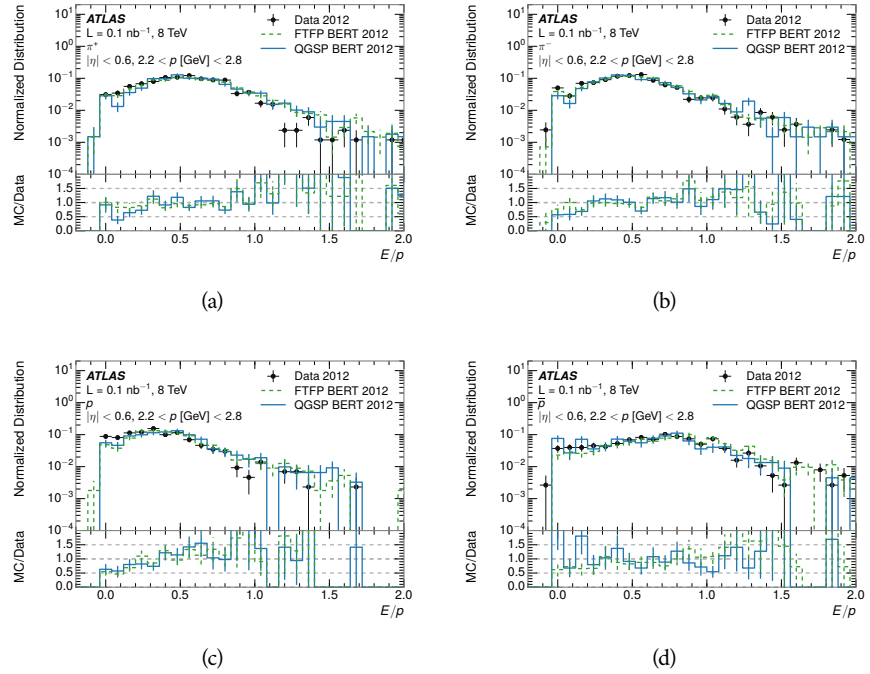


Figure 14: The  $E/p$  distribution for isolated (a)  $\pi^+$ , (b)  $\pi^-$ , (c) proton, and (d) anti-proton tracks.

619        The zero fraction is further explored in Figure 15 for pions and protons in  
 620        data and simulation. The simulation consistently underestimates the zero frac-  
 621        tion independent of particle species, which implies that this discrepancy is not  
 622        caused by the model of a particular species but rather a feature common to all.

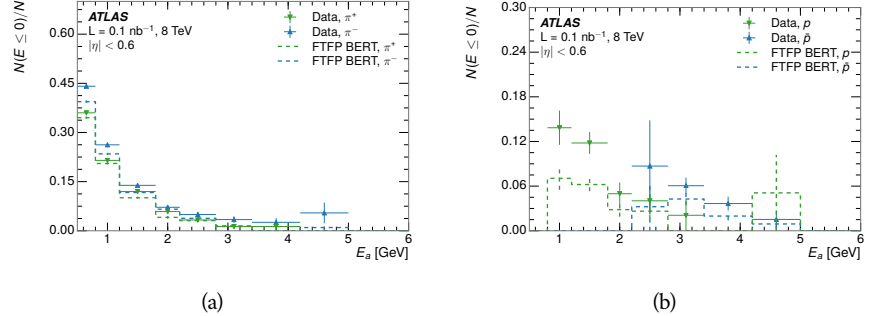


Figure 15: The fraction of tracks with  $E \leq 0$  for identified (a)  $\pi^+$  and  $\pi^-$ , and (b) proton and anti-proton tracks

623        It is also interesting to compare the response between the different particle  
 624        species. One approach to do this is to measure the difference in  $\langle E/p \rangle$  between  
 625        two types, which has the advantage of removing the neutral background. These  
 626        differences are shown in various combinations in Figure 16. The response for  
 627         $\pi^+$  is greater on average than the response to  $\pi^-$  because of a charge-exchange  
 628        effect which causes the production of additional neutral pions in the showers of  
 629         $\pi^+$  [20]. The response for  $\pi^+$  is also greater on average than the response to  $p$ ,

630 because a large fraction of the energy of  $\pi^+$  hadrons is converted to an electro-  
 631 magnetic shower [11, 25]. However, the  $\bar{p}$  response is significantly higher than  
 632 the response to  $\pi^-$  because of the annihilation of the antiproton. FTFP\_BERT  
 633 does a better job of modeling this effect than QGSP\_BERT because of their differ-  
 634 ent descriptions of  $\bar{p}$  interactions with material.

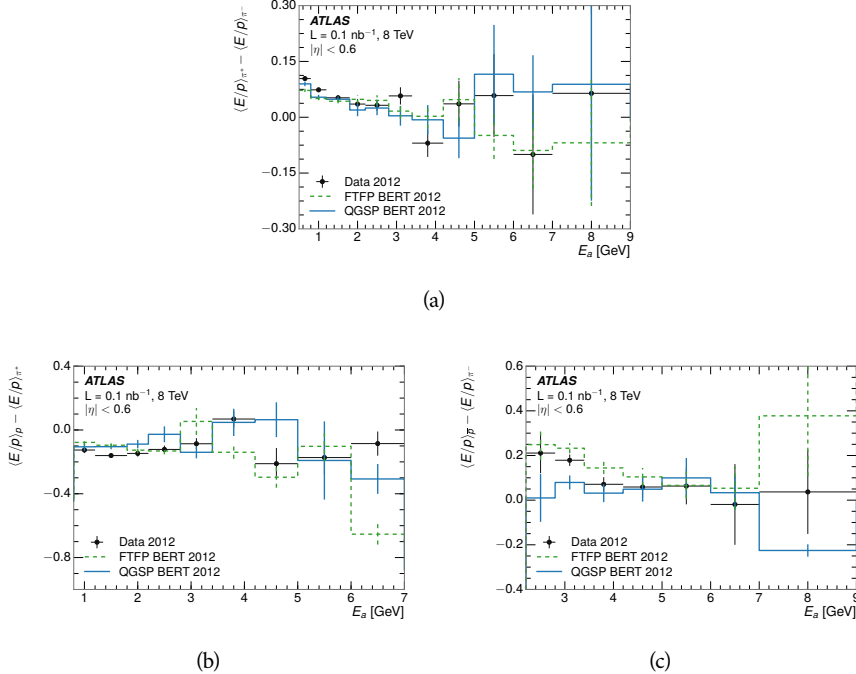


Figure 16: The difference in  $\langle E/p \rangle$  between (a)  $\pi^+$  and  $\pi^-$  (b)  $p$  and  $\pi^+$ , and (c)  $\bar{p}$  and  $\pi^-$ .

635 It is also possible to remove the neutral background from these response dis-  
 636 tributions using the same technique as in Section 8.2.3. The technique is largely  
 637 independent of the particle species and so can be directly applied to  $\langle E/p \rangle$  for  
 638 pions. The  $\langle E/p \rangle_{\text{COR}}$  distributions for pions are shown in Figure 17, which are  
 639 very similar to the inclusive results. The inclusive hadrons are compromised  
 640 mostly of pions, so this similarity is not surprising. It is also possible to see the  
 641 small differences between  $\pi^+$  and  $\pi^-$  response here, where  $\langle E/p \rangle_{\text{COR}}$  is higher  
 642 on average for  $\pi^+$ . The agreement between data and simulation is significantly  
 643 worse for the  $\pi^-$  distributions than for the  $\pi^+$ , with a discrepancy greater than  
 644 10% below 2-3 GeV.

#### 645 8.3.3 ADDITIONAL SPECIES IN SIMULATION

646 The techniques above provide a method to measure the response separately only  
 647 pions and protons. However the hadrons which forms jets include a number of  
 648 additional species such as kaons and neutrons. The charged kaons are an impor-  
 649 tant component of the inclusive charged hadron distribution, which is compro-  
 650 mised of roughly 60-70% pions, 15-20% kaons, and 5-15% protons. These are dif-  
 651 ficult to measure in data at the ATLAS detector, although a template subtraction

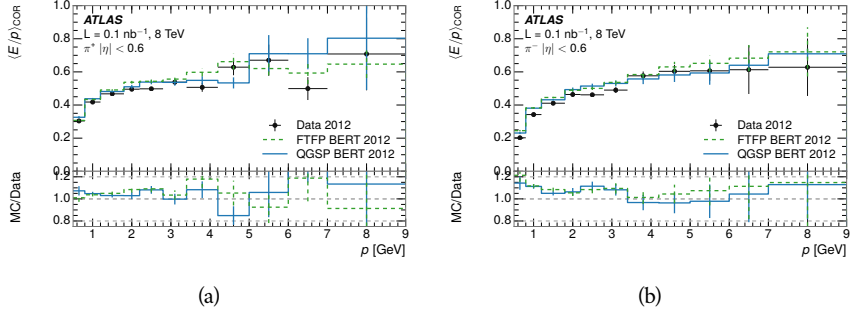


Figure 17:  $\langle E/p \rangle_{\text{COR}}$  as a function of track momentum for (a)  $\pi^+$  tracks and (b)  $\pi^-$  tracks.

technique has been proposed which may be effective with larger sample sizes [8].  
The simulation of these particles includes noticeable differences in response at  
low energies, which are shown in Figure 18 for FTFP\_BERT. The significant differ-  
ences in response between low energy protons and antiprotons are accounted  
for above in the definitions of  $E_a$ .

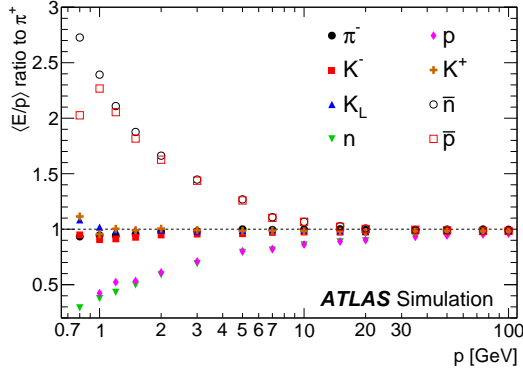


Figure 18: The ratio of the calorimeter response to single particles of various species to the calorimeter response to  $\pi^+$  with the physics list FTFP\_BERT.

#### 8.4 SUMMARY

These various measurements of calorimeter response shown above for data and simulation illuminate the accuracy of the simulation of hadronic interactions at the ATLAS detector. The results were done using 2010 and 2012 data at 7 and 8 TeV, but reflect the most current understanding of the detector alignment and geometry. A number of measurements focusing on a comparison between protons and antiprotons suggest that FTFP\_BERT models those interaction more accurately than QGSP\_BERT. These measurements, among others, were the motivation to switch the default Geant4 simulation from FTFP\_BERT to QGSP\_BERT for all ATLAS samples.

Even with these updates, there are a number of small, approximately 5%, discrepancies in response between the data and simulation at low energies. At higher

669 energies the simulation of hadronic interactions is very consistent with data.  
670 Chapter 9 discusses how to use these observed differences to constrain the jet  
671 energy scale and its associated uncertainties.



672

## 673 JET ENERGY RESPONSE AND UNCERTAINTY

## 674 9.1 MOTIVATION

675 As jets form a major component of many physics analyses at ATLAS, it is crucial  
 676 to carefully calibrate the measurement of jet energies and to derive an uncer-  
 677 tainty on that measurement. These uncertainties have often been the dominant  
 678 systematic uncertainty in high-energy analyses at the LHC. Dijet and multijet bal-  
 679 ance techniques provide a method to constrain the jet energy scale and its uncer-  
 680 tainty in data, and provide the default values used for ATLAS jet measurements  
 681 at most energies [7]. These techniques are limited by their reliance on measuring  
 682 jets in data, so they are statistically limited in estimating the jet energy scale at the  
 683 highest jet energies. This chapter presents another method for estimating the jet  
 684 energy scale and its uncertainty which builds up a jet from its components and  
 685 thus can be naturally extended to high jet momentum. Throughout this chapter  
 686 the jets studied are simulated using Pythia8 with the CT10 parton distribution  
 687 set [27] and the AU2 tune [3], and corrections are taken from the studies includ-  
 688 ing data and simulation in Chapter 8.

689 As described in Section 7.2, jets are formed from topological clusters of energy  
 690 in the calorimeters using the anti- $k_t$  algorithm. These clusters originate from a  
 691 diverse spectrum of particles, in terms of both species and momentum, leading to  
 692 significantly varied jet properties and response between jets of similar produced  
 693 momentum. Figure 19 shows the simulated distribution of particles within jets  
 694 at a few examples energies. The  $E/p$  measurements provide a thorough under-  
 695 standing of the dominant particle content of jets, the charged hadrons.

## 696 9.2 UNCERTAINTY ESTIMATE

697 Simulated jets are not necessarily expected to correctly model the energy de-  
 698 posits in the calorimeters, because of the various discrepancies discussed in Chap-  
 699 ter 8. To evaluate a jet energy response, the simulated jet energies are compared  
 700 to a corrected jet built up at the particle level. Each cluster in a jet is associated  
 701 to the truth particle which deposited it, and the energy in that cluster is then  
 702 corrected for a number of effects based on measurements in data. The primary  
 703 corrections come from the single hadron response measurements in addition  
 704 to response measured using the combined test beam which covers higher mo-  
 705 mentum particles [10]. These corrections include both a shift, in order to make  
 706 the simulation match the average response in data, and an uncertainty associated  
 707 with the ability to constrain the difference between data and simulation. Some of  
 708 the dominant sources of uncertainty are itemized below, and the full list consid-  
 709 ered is described in detail in the associated paper [8]. These uncertainties cover

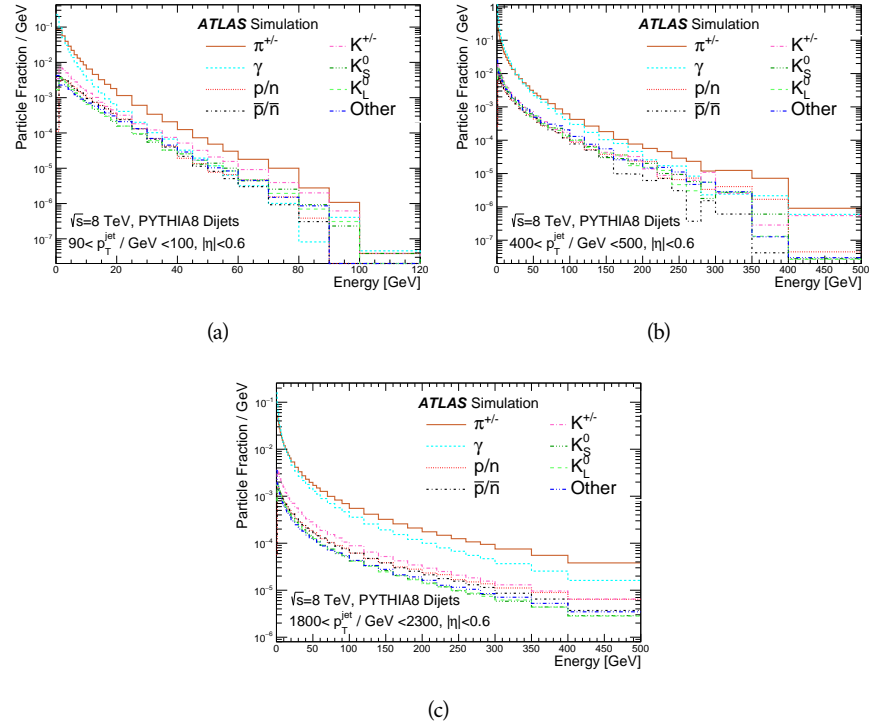


Figure 19: The spectra of true particles inside anti- $k_t$ ,  $R = 0.4$  jets with (a)  $90 < p_T/\text{GeV} < 100$ , (b)  $400 < p_T/\text{GeV} < 500$ , and (c)  $1800 < p_T/\text{GeV} < 2300$ .

710 differences between the data and simulation in the modeling of calorimeter re-  
 711 sponse to a given particle. No uncertainties are added for the difference between  
 712 particle composition of jets in data and simulation.

- 713 • The comparison of  $\langle E/p \rangle_{\text{COR}}$  as described in Chapter 8 with statistical  
 714 uncertainties from 500 MeV to 20 GeV (“In situ  $E/p$ ”).
- 715 • The main  $\langle E/p \rangle$  comparison uncertainties, binned in  $p$  and  $|\eta|$ , as derived  
 716 from the combined test beam results, from 20 to 350 GeV (“CTB” from  
 717 Ref. [10]).
- 718 • The difference in the zero-fraction between data and MC simulation from  
 719 500 MeV to 20 GeV (“ $E/p$  Zero Fraction”).
- 720 • The uncertainty in the EM calorimeter response from the potential mis-  
 721 modelling of threshold effects in topological clustering (“ $E/p$  Threshold”).
- 722 • The uncertainty in the calorimeter response to neutral hadrons based on  
 723 studies of physics model variations (“Neutral”).
- 724 • An additional uncertainty in the response to neutral  $K_L$  in the calorimeter  
 725 based on studies of physics model variations (“ $K_L$ ”).
- 726 • The uncertainty in the  $p$  measurement from misalignment of the ID (“ $E/p$   
 727 Misalignment”).

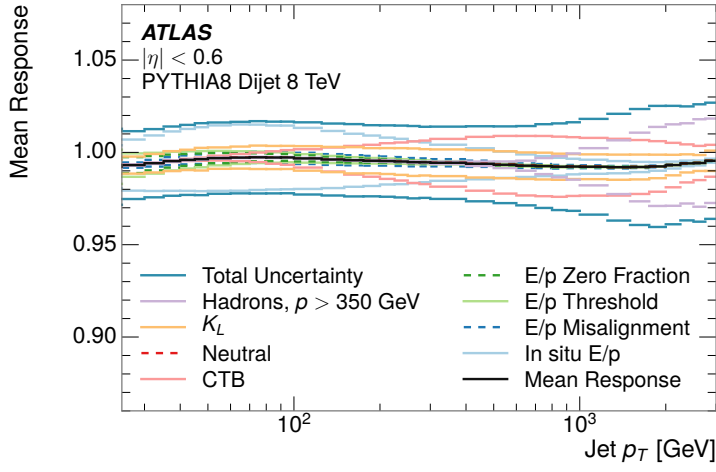
- 728 • A flat uncertainty for all particles above the energy range or outside the  
 729 longitudinal range probed with the combined test beam (“Hadrons,  $p >$   
 730 350 GeV”).

731 From these terms, the jet energy scale and uncertainty is built up from individual  
 732 energy deposits in simulation. Each uncertainty term is treated independently,  
 733 and are taken to be gaussian distributed. The resulting scale and uncertainty  
 734 is shown in Figure 20, where the mean response is measured relative to the  
 735 calibrated energy reported by simulation. The dominant uncertainties come  
 736 from the statistical uncertainties on the  $E/p$  measurements at lower energies and  
 737 the additional uncertainty for out of range measurements at higher energies. The  
 738 total uncertainty from this method at intermediate jet energies is comparable to  
 739 other simulation-based methods [4] and is about twice as large as in-situ meth-  
 740 ods using data [7]. This method is the only one which provides an estimation  
 741 above 1.8 TeV, however, and so is still a crucial technique in analyses that search  
 742 for very energetic jets.

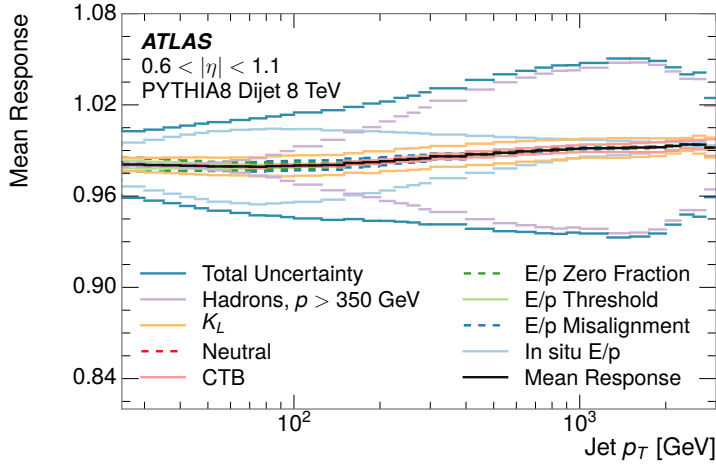
743 These techniques can also be used to measure the correlation between the  
 744 average reconstructed jet momentum in a given bin of  $p_T$  and  $|\eta|$ , where cor-  
 745 relations are expected because of a similarity in particle composition at similar  
 746 energies. Figure 21 shows these correlations, where the uncertainties on jets in  
 747 neighboring bins are typically between 30% and 60% correlated. The uncertainty  
 748 on all jets becomes significantly correlated at high energies and larger pseudora-  
 749 pidities, when the uncertainty becomes dominated by the single term reflecting  
 750 out of range particles.

### 751 9.3 SUMMARY

752 The technique described above provides a jet energy scale and uncertainty by  
 753 building up jet corrections from the energy deposits of constituent particles. The  
 754  $E/p$  measurements are crucial in providing corrections for the majority of parti-  
 755 cles in the jets. The uncertainty derived this way is between 2 and 5% and is about  
 756 twice as large at corresponding momentum than jet balance methods. However  
 757 this is the only uncertainty available for very energetic jets using 2012 data and  
 758 simulation, and repeating this method with Run 2 data and simulation will be  
 759 important in providing an uncertainty for the most energetic jets in 13 TeV col-  
 760 lisions.



(a)



(b)

Figure 20: The jet energy scale uncertainty contributions, as well as the total jet energy scale uncertainty, as a function of jet  $p_T$  for (a)  $|\eta| < 0.6$  and (b)  $0.6 < |\eta| < 1.1$ .

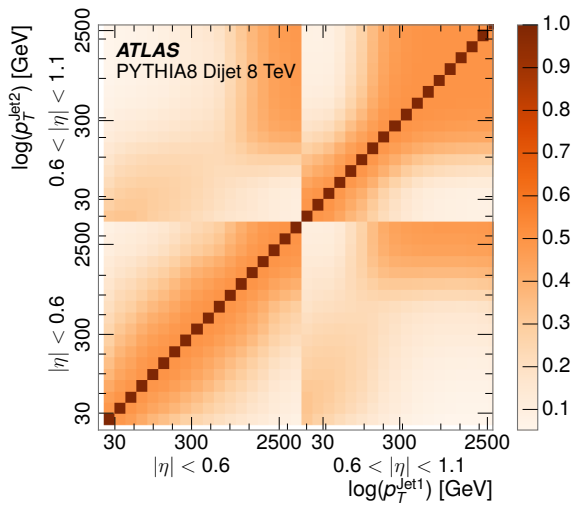


Figure 21: The jet energy scale correlations as a function of jet  $p_T$  and  $|\eta|$  for jets in the central region of the detector.



761

## PART V

762

### SEARCH FOR LONG-LIVED PARTICLES

763

You can put some informational part preamble text here.



# 10

764

765 LONG-LIVED PARTICLES IN ATLAS

---

766 10.1 OVERVIEW AND CHARACTERISTICS

767 10.2 SIMULATION



768

769 EVENT SELECTION

---

770 11.1 TRIGGER

771 11.2 KINEMATICS AND ISOLATION

772 11.3 STANDARD MODEL REJECTION

773 11.4 IONIZATION

774 11.4.1 DE/DX CALIBRATION

775 11.4.2 MASS ESTIMATION



# 12

776

777 BACKGROUND ESTIMATION

---

778 12.1 BACKGROUND SOURCES

779 12.2 PREDICTION METHOD

780 12.3 VALIDATION AND UNCERTAINTY



# 13

781

782 SYSTEMATIC UNCERTAINTIES AND RESULTS

---

783 13.1 SYSTEMATIC UNCERTAINTIES

784 13.2 FINAL YIELDS



# 14

785

## 786 INTERPRETATION

---

787 14.1 CROSS SECTIONAL LIMITS

788 14.2 MASS LIMITS

789 14.3 CONTEXT FOR LONG-LIVED SEARCHES



790

## PART VI

791

### CONCLUSIONS

792

You can put some informational part preamble text here.



# 15

793

794 SUMMARY AND OUTLOOK

---

795 15.1 SUMMARY

796 15.2 OUTLOOK



797

## PART VII

798

## APPENDIX

799



# A

800

801 INELASTIC CROSS SECTION

---



# B

802

## 803 APPENDIX TEST

---

804 Examples: *Italics*, SMALL CAPS, ALL CAPS <sup>1</sup>. Acronym testing: **UML!** (**UML!**) –  
805 **UML! – UML! (UML!) – UML!s**

*This appendix is temporary and is here to be used to check the style of the document.*

### 806 B.1 APPENDIX SECTION TEST

807 Random text that should take up a few lines. The purpose is to see how sections  
808 and subsections flow with some actual context. Without some body copy be-  
809 tween each heading it can be difficult to tell if the weight of the fonts, styles,  
810 and sizes use work well together.

#### 811 B.1.1 APPENDIX SUBECTION TEST

812 Random text that should take up a few lines. The purpose is to see how sections  
813 and subsections flow with some actual context. Without some body copy be-  
814 tween each heading it can be difficult to tell if the weight of the fonts, styles,  
815 and sizes use work well together.

### 816 B.2 A TABLE AND LISTING

817 Curabitur tellus magna, porttitor a, commodo a, commodo in, tortor. Donec in-  
818 terdum. Praesent scelerisque. Maecenas posuere sodales odio. Vivamus metus la-  
819 cus, varius quis, imperdiet quis, rhoncus a, turpis. Etiam ligula arcu, elementum a,  
820 venenatis quis, sollicitudin sed, metus. Donec nunc pede, tincidunt in, venenatis  
821 vitae, faucibus vel, nibh. Pellentesque wisi. Nullam malesuada. Morbi ut tellus ut  
822 pede tincidunt porta. Lorem ipsum dolor sit amet, consectetur adipiscing elit.  
823 Etiam congue neque id dolor.

824 There is also a Python listing below Listing 1.

---

1 Footnote example.

LABITUR BONORUM PRI NO	QUE VISTA	HUMAN
fastidii ea ius	germano	demonstratea
suscipit instructior	titulo	personas
quaestio philosophia	facto	demonstrated

Table 1: Autem usu id.

## 825 B.3 SOME FORMULAS

Due to the statistical nature of ionisation energy loss, large fluctuations can occur in the amount of energy deposited by a particle traversing an absorber element<sup>2</sup>. Continuous processes such as multiple scattering and energy loss play a relevant role in the longitudinal and lateral development of electromagnetic and hadronic showers, and in the case of sampling calorimeters the measured resolution can be significantly affected by such fluctuations in their active layers. The description of ionisation fluctuations is characterised by the significance parameter  $\kappa$ , which is proportional to the ratio of mean energy loss to the maximum allowed energy transfer in a single collision with an atomic electron:

*You might get unexpected results using math in chapter or section heads. Consider the pdfspacing option.*

$$\kappa = \frac{\xi}{E_{\max}} \quad (1)$$

$E_{\max}$  is the maximum transferable energy in a single collision with an atomic electron.

$$E_{\max} = \frac{2m_e\beta^2\gamma^2}{1 + 2\gamma m_e/m_x + (m_e/m_x)^2},$$

826 where  $\gamma = E/m_x$ ,  $E$  is energy and  $m_x$  the mass of the incident particle,  $\beta^2 =$   
 827  $1 - 1/\gamma^2$  and  $m_e$  is the electron mass.  $\xi$  comes from the Rutherford scattering  
 828 cross section and is defined as:

$$\xi = \frac{2\pi z^2 e^4 N_{Av} Z \rho \delta x}{m_e \beta^2 c^2 A} = 153.4 \frac{z^2}{\beta^2} \frac{Z}{A} \rho \delta x \text{ keV},$$

829 where

830  $z$  charge of the incident particle  
 830  $N_{Av}$  Avogadro's number  
 830  $Z$  atomic number of the material  
 830  $A$  atomic weight of the material  
 830  $\rho$  density  
 830  $\delta x$  thickness of the material  
 831  $\kappa$  measures the contribution of the collisions with energy transfer close to  
 832  $E_{\max}$ . For a given absorber,  $\kappa$  tends towards large values if  $\delta x$  is large and/or if  
 833  $\beta$  is small. Likewise,  $\kappa$  tends towards zero if  $\delta x$  is small and/or if  $\beta$  approaches  
 834 1.

2 Examples taken from Walter Schmidt's great gallery:  
<http://home.vrweb.de/~was/mathfonts.html>

Listing 1: A floating example (listings manual)

---

```
1 for i in xrange(10):
    print i, i*i, i*i*i
print "done"
```

---

835        The value of  $\kappa$  distinguishes two regimes which occur in the description of  
836        ionisation fluctuations:

- 837        1. A large number of collisions involving the loss of all or most of the incident  
838        particle energy during the traversal of an absorber.

839        As the total energy transfer is composed of a multitude of small energy  
840        losses, we can apply the central limit theorem and describe the fluctua-  
841        tions by a Gaussian distribution. This case is applicable to non-relativistic  
842        particles and is described by the inequality  $\kappa > 10$  (i. e., when the mean  
843        energy loss in the absorber is greater than the maximum energy transfer  
844        in a single collision).

- 845        2. Particles traversing thin counters and incident electrons under any condi-  
846        tions.

847        The relevant inequalities and distributions are  $0.01 < \kappa < 10$ , Vavilov  
848        distribution, and  $\kappa < 0.01$ , Landau distribution.



- 850 [1] ATLAS Collaboration. “The ATLAS Simulation Infrastructure”. In: *Eur.*  
851 *Phys. J. C* 70 (2010), p. 823. doi: [10.1140/epjc/s10052-010-1429-9](https://doi.org/10.1140/epjc/s10052-010-1429-9).  
852 arXiv: [1005.4568 \[hep-ex\]](https://arxiv.org/abs/1005.4568). SOFT-2010-01.
- 853 [2] ATLAS Collaboration. “A study of the material in the ATLAS inner de-  
854 tector using secondary hadronic interactions”. In: *JINST* 7 (2012), P01013.  
855 doi: [10.1088/1748-0221/7/01/P01013](https://doi.org/10.1088/1748-0221/7/01/P01013). arXiv: [1110.6191 \[hep-ex\]](https://arxiv.org/abs/1110.6191).  
856 PERF-2011-08.
- 857 [3] ATLAS Collaboration. *Summary of ATLAS Pythia 8 tunes*. ATL-PHYS-PUB-  
858 2012-003. 2012. url: <http://cds.cern.ch/record/1474107>.
- 859 [4] ATLAS Collaboration. “Jet energy measurement with the ATLAS detector  
860 in proton–proton collisions at  $\sqrt{s} = 7$  TeV”. In: *Eur. Phys. J. C* 73 (2013),  
861 p. 2304. doi: [10.1140/epjc/s10052-013-2304-2](https://doi.org/10.1140/epjc/s10052-013-2304-2). arXiv: [1112.6426 \[hep-ex\]](https://arxiv.org/abs/1112.6426). PERF-2011-03.
- 863 [5] ATLAS Collaboration. “Single hadron response measurement and calorime-  
864 ter jet energy scale uncertainty with the ATLAS detector at the LHC”. In:  
865 *Eur. Phys. J. C* 73 (2013), p. 2305. doi: [10.1140/epjc/s10052-013-2305-1](https://doi.org/10.1140/epjc/s10052-013-2305-1). arXiv: [1203.1302 \[hep-ex\]](https://arxiv.org/abs/1203.1302). PERF-2011-05.
- 867 [6] ATLAS Collaboration. “Electron and photon energy calibration with the  
868 ATLAS detector using LHC Run 1 data”. In: *Eur. Phys. J. C* 74 (2014), p. 3071.  
869 doi: [10.1140/epjc/s10052-014-3071-4](https://doi.org/10.1140/epjc/s10052-014-3071-4). arXiv: [1407.5063 \[hep-ex\]](https://arxiv.org/abs/1407.5063). PERF-2013-05.
- 871 [7] ATLAS Collaboration. “Jet energy measurement and its systematic uncer-  
872 tainty in proton–proton collisions at  $\sqrt{s} = 7$  TeV with the ATLAS detec-  
873 tor”. In: *Eur. Phys. J. C* 75 (2015), p. 17. doi: [10.1140/epjc/s10052-014-3190-y](https://doi.org/10.1140/epjc/s10052-014-3190-y). arXiv: [1406.0076 \[hep-ex\]](https://arxiv.org/abs/1406.0076). PERF-2012-01.
- 875 [8] ATLAS Collaboration. “A measurement of the calorimeter response to sin-  
876 ggle hadrons and determination of the jet energy scale uncertainty using  
877 LHC Run-1  $pp$ -collision data with the ATLAS detector”. In: (2016). arXiv:  
878 [1607.08842 \[hep-ex\]](https://arxiv.org/abs/1607.08842). PERF-2015-05.
- 879 [9] ATLAS Collaboration. “Topological cell clustering in the ATLAS calorime-  
880 ters and its performance in LHC Run 1”. In: (2016). arXiv: [1603.02934 \[hep-ex\]](https://arxiv.org/abs/1603.02934).
- 882 [10] E. Abat et al. “Study of energy response and resolution of the ATLAS barrel  
883 calorimeter to hadrons of energies from 20 to 350 GeV”. In: *Nucl. Instrum.*  
884 *Meth. A* 621.1-3 (2010), pp. 134 – 150. doi: <http://dx.doi.org/10.1016/j.nima.2010.04.054>.

- 886 [11] P. Adragna et al. "Measurement of Pion and Proton Response and Lon-  
 887 gitudinal Shower Profiles up to 20 Nuclear Interaction Lengths with the  
 888 ATLAS Tile Calorimeter". In: *Nucl. Instrum. Meth. A* 615 (2010), pp. 158–  
 889 181. doi: [10.1016/j.nima.2010.01.037](https://doi.org/10.1016/j.nima.2010.01.037).
- 890 [12] S. Agostinelli et al. "GEANT4: A simulation toolkit". In: *Nucl. Instrum. Meth.*  
 891 A 506 (2003), pp. 250–303. doi: [10.1016/S0168-9002\(03\)01368-8](https://doi.org/10.1016/S0168-9002(03)01368-8).
- 892 [13] N. S. Amelin et al. "Transverse flow and collectivity in ultrarelativistic  
 893 heavy-ion collisions". In: *Phys. Rev. Lett.* 67 (1991), p. 1523. doi: [10.1103/PhysRevLett.67.1523](https://doi.org/10.1103/PhysRevLett.67.1523).
- 895 [14] N. S. Amelin et al. "Collectivity in ultrarelativistic heavy ion collisions". In:  
 896 *Nucl. Phys. A* 544 (1992), p. 463. doi: [10.1016/0375-9474\(92\)90598-E](https://doi.org/10.1016/0375-9474(92)90598-E).
- 898 [15] B. Andersson, A. Tai, and B.-H. Sa. "Final state interactions in the (nuclear)  
 899 FRITIOF string interaction scenario". In: *Z. Phys. C* 70 (1996), pp. 499–  
 900 506. doi: [10.1007/s002880050127](https://doi.org/10.1007/s002880050127).
- 901 [16] B. Andersson et al. "A model for low-pT hadronic reactions with general-  
 902 izations to hadron-nucleus and nucleus-nucleus collisions". In: *Nucl. Phys.*  
 903 B 281 (1987), p. 289. doi: [10.1016/0550-3213\(87\)90257-4](https://doi.org/10.1016/0550-3213(87)90257-4).
- 904 [17] H. W. Bertini and P. Guthrie. "News item results from medium-energy  
 905 intranuclear-cascade calculation". In: *Nucl. Instr. and Meth. A* 169 (1971),  
 906 p. 670. doi: [10.1016/0375-9474\(71\)90710-X](https://doi.org/10.1016/0375-9474(71)90710-X).
- 907 [18] L. V. Bravin et al. "Scaling violation of transverse flow in heavy ion col-  
 908 lisions at AGS energies". In: *Phys. Lett. B* 344 (1995), p. 49. doi: [10.1016/0370-2693\(94\)01560-Y](https://doi.org/10.1016/0370-2693(94)01560-Y).
- 910 [19] L. V. Bravina et al. "Fluid dynamics and Quark Gluon string model - What  
 911 we can expect for Au+Au collisions at 11.6 AGeV/c". In: *Nucl. Phys. A* 566  
 912 (1994), p. 461. doi: [10.1016/0375-9474\(94\)90669-6](https://doi.org/10.1016/0375-9474(94)90669-6).
- 913 [20] CMS Collaboration. "The CMS barrel calorimeter response to particle  
 914 beams from 2 to 350 GeV/c". In: *Eur. Phys. J. C* 60.3 (2009). doi: [10.1140/epjc/s10052-009-0959-5](https://doi.org/10.1140/epjc/s10052-009-0959-5).
- 916 [21] H. S. Fesefeldt. *GHEISHA program*. Pitha-85-02, Aachen. 1985.
- 917 [22] G. Folger and J.P. Wellisch. "String parton models in Geant4". In: (2003).  
 918 arXiv: [nucl-th/0306007](https://arxiv.org/abs/nucl-th/0306007).
- 919 [23] B. Ganhuyag and V. Uzhinsky. "Modified FRITIOF code: Negative charged  
 920 particle production in high energy nucleus nucleus interactions". In: *Czech.*  
 921 *J. Phys.* 47 (1997), pp. 913–918. doi: [10.1023/A:1021296114786](https://doi.org/10.1023/A:1021296114786).
- 922 [24] M. P. Guthrie, R. G. Alsmiller, and H. W. Bertini. "Calculation of the cap-  
 923 ture of negative pions in light elements and comparison with experiments  
 924 pertaining to cancer radiotherapy". In: *Nucl. Instrum. Meth.* 66 (1968), pp. 29–  
 925 36. doi: [10.1016/0029-554X\(68\)90054-2](https://doi.org/10.1016/0029-554X(68)90054-2).
- 926 [25] J. Beringer et al. (Particle Data Group). "Review of Particle Physics". In:  
 927 *Chin. Phys. C* 38 (2014), p. 090001. URL: <http://pdg.lbl.gov>.

- 928 [26] V.A. Karmanov. "Light Front Wave Function of Relativistic Composite  
929 System in Explicitly Solvable Model". In: *Nucl. Phys. B* 166 (1980), p. 378.  
930 doi: [10.1016/0550-3213\(80\)90204-7](https://doi.org/10.1016/0550-3213(80)90204-7).
- 931 [27] Hung-Liang Lai, Marco Guzzi, Joey Huston, Zhao Li, Pavel M. Nadolsky,  
932 et al. "New parton distributions for collider physics". In: *Phys. Rev. D* 82  
933 (2010), p. 074024. doi: [10.1103/PhysRevD.82.074024](https://doi.org/10.1103/PhysRevD.82.074024). arXiv: [1007.2241 \[hep-ph\]](https://arxiv.org/abs/1007.2241).
- 935 [28] A.D. Martin, W.J. Stirling, R.S. Thorne, and G. Watt. "Parton distributions  
936 for the LHC". In: *Eur. Phys. J. C* 63 (2009). Figures from the [MSTW Website](#),  
937 pp. 189–285. doi: [10.1140/epjc/s10052-009-1072-5](https://doi.org/10.1140/epjc/s10052-009-1072-5). arXiv: [0901.0002](https://arxiv.org/abs/0901.0002).
- 939 [29] B. Nilsson-Almqvist and E. Stenlund. "Interactions Between Hadrons and  
940 Nuclei: The Lund Monte Carlo, Fritiof Version 1.6". In: *Comput. Phys. Com-*  
941 *mun.* 43 (1987), p. 387. doi: [10.1016/0010-4655\(87\)90056-7](https://doi.org/10.1016/0010-4655(87)90056-7).
- 942 [30] A. Ribon et al. *Status of Geant4 hadronic physics for the simulation of LHC*  
943 *experiments at the start of LHC physics program.* CERN-LCGAPP-2010-02.  
944 2010. URL: <http://lcgapp.cern.ch/project/docs/noteStatusHadronic2010.pdf>.
- 946 [31] A. Sherstnev and R.S. Thorne. "Parton Distributions for LO Generators".  
947 In: *Eur. Phys. J. C* 55 (2008), pp. 553–575. doi: [10.1140/epjc/s10052-008-0610-x](https://doi.org/10.1140/epjc/s10052-008-0610-x). arXiv: [0711.2473](https://arxiv.org/abs/0711.2473).
- 949 [32] T. Sjöstrand, S. Mrenna, and P. Skands. "A Brief Introduction to PYTHIA  
950 8.1". In: *Comput. Phys. Commun.* 178 (2008), pp. 852–867. doi: [10.1016/j.cpc.2008.01.036](https://doi.org/10.1016/j.cpc.2008.01.036). arXiv: [0710.3820](https://arxiv.org/abs/0710.3820).
- 952 [33] Peter Speckmayer. "Energy Measurement of Hadrons with the CERN AT-  
953 LAS Calorimeter". Presented on 18 Jun 2008. PhD thesis. Vienna: Vienna,  
954 Tech. U., 2008. URL: <http://cds.cern.ch/record/1112036>.



955 DECLARATION

---

956 Put your declaration here.

957 *Berkeley, CA, September 2016*

958

---

Bradley Axen



959

960 COLOPHON

961

Not sure that this is necessary.